Full Length Article

Oxygen-terminated diamond: insights into the correlation between surface oxygen configurations and work function values

Ramiz Zulkharnay [*], Gulnur Zulpukarova , Paul W. May

School of Chemistry, University of Bristol, Cantock's Close, Bristol BS8 1TS, United Kingdom

ABSTRACT

The surface modification of diamond holds crucial significance in various applications, such as electron emission devices, Schottky diodes and field-effect transistors. Oxygen termination is one of the most common termination types, where three distinct carbon-oxygen bonded configurations (*i.e.* ether, ketone and hydroxyl) are typically found concurrently on the surface. An unanswered question in this context is whether each oxygen-containing functional group influences the tuning of the surface electronic properties of diamond. Here, we systematically explore the surface oxidation of (100)-oriented single-crystal diamond using four different oxidation methods: oxygen plasma exposure, UV-ozone irradiation, acid treatment and oxygen-gas thermal cracking. The relative concentration of the oxygen functional groups varies significantly depending upon the oxidation technique used. Specifically, O_2-plasma and thermal-cracking methods result in higher percentages of ether configurations (52.1% and 71.5%, respectively), whereas UV-ozone and acid-oxidation treatments preferentially yield ketone (47.9%) and hydroxyl (51.3%) groups. Additionally, employing state-of-the-art surface-science techniques, the surface electronic structure of each oxygenated sample is revealed. These experimental findings show that specific oxidation methods significantly alter the work function of *all* four oxidised surfaces, being measured in the range of 4.65 eV and 5.79 eV. This study paves the way towards selective tuning of the oxygen surface configurations suitable for fabricating diamond-based energy materials.

1. Introduction

Surface functionalisation of diamond has gained growing significance in a diverse array of emerging applications, including DNA sensing [1,2], quantum engineering [3–5] and power harvesting [6–8]. Most efforts aimed at surface modification of diamond predominantly focus on terminating the surface with hydrogen or oxygen, although other alternative adsorbates have been reported to modify the surface for different applications [7]. When the surface is terminated with H atoms, diamond exhibits a negative electron affinity (NEA) of approximately -1.3 eV [9,10]. This intriguing property positions the vacuum level beneath the conduction band minimum (CBM), eliminating any potential barrier for emission from the surface of electrons located within the CB. This unusual NEA surface allows diamond to act as an efficient source of ejected electrons *in vacuo*, enabling exciting opportunities for a diverse range of energy-related devices [11–13].

However, H-termination on diamond can be readily replaced by O atoms, eliminating the surface conductivity, reducing surface charge transfer, and ultimately resulting in a shift in polarity to positive

electron affinity (PEA) [9]. Diamond oxidation is typically achieved through varied techniques, such as exposure to an O_2 plasma, a UV-ozone lamp in air, treatment with strong acids, thermal annealing in air or electrochemical oxidation [14–18]. Although the PEA surface is detrimental to electron emission, such oxygen-terminated diamond surfaces have applications as electrochemical electrodes [19,20] and are the preferred termination for biological cell attachment and culturing [21–23].

Depending on the oxidation technique used, various bonding configurations can be realised between oxygen and the surface carbon atoms of diamond, denoted as C_d. While these diverse bonding motifs generally encompass the formation of ketone (C_d=O), bridging ether (C_d–O–C_d) and hydroxyl (C_d–OH), their relative concentrations are substantially altered by the particular oxidation method used. Moreover, the limited understanding of and the difficulty in controlling the ratio of ketone : ether : hydroxyl in the oxygenated surface have recently rendered studies of the metal–O–C_d system particularly challenging [24,25]. Hence, a thorough experimental investigation of the O-terminated surface in single-crystal diamond (SCD) in order to elucidate the

oxidation degree and resulting surface arrangements has yet to be reported.

In this study, we present a systematic investigation of the surface oxidation of SCD (100) using a variety of oxidative techniques, including O_2 plasma exposure, UV-ozone and acid treatments, and thermal cracking of O_2. The surface electronic properties of variously oxidised diamond surfaces were characterised by X-ray and ultraviolet-photoelectron spectroscopy (XPS and UPS, respectively), real and reciprocal mapping by energy-filtered photoemission electron microscopy (EF-PEEM), and spot-profile analysis low-energy electron diffraction (SPA-LEED) measurements.

2. Experimental section

2.1. Sample preparation

Free-standing SCD (100) diamond substrates (product code: 145-500-0547) purchased from Element Six, Ltd (Ascot, UK) were first subjected to a boiling mixture of concentrated sulfuric acid with potassium nitrate (6.5 g KNO_3 in 100 ml of 95% H_2SO_4) for 3 h to clean the surface from polishing-induced contaminants. The clean substrates were then capped by deposition of an epitaxial conductive ~0.5 µm boron-doped diamond (BDD) overlayer (with a boron concentration of ~10^{20} cm^{-3}) using a bespoke hot-filament chemical vapour deposition (HF-CVD) reactor. The CVD process employed a gas mixture comprising 1% CH_4 and 5% B_2H_6 in H_2 (with a B:C ratio of 1250 ppm) with a total gas flow of 202.1 standard cubic centimetres per minute (sccm), regulated by separate mass flow controllers. A hot tantalum filament (>2000 °C) facilitated the thermal decomposition of the gases into reactive atoms and radicals under 20 Torr [10]. The resultant thin conductive layer was necessary to avoid surface charging in subsequent XPS experiments [10,24,25]. Although this short CVD step produced films with an H termination, a delay of several days/weeks before subsequent XPS analysis meant that the diamond surfaces may have oxidised slightly from the ambient air. Thus, before each oxidation experiment, the surfaces were re-hydrogenated using a microwave plasma-enhanced CVD reactor (MPE-CVD), as described in Ref. [10] to ensure an identical hydrogenated starting surface in each case. Each of the 4 hydrogenated sample then immediately underwent a different *ex situ* oxidation treatment.

The first oxidation method involved exposing the sample to an O_2 DC plasma in a modified sputter-coater (Edwards S150A) at 65 W for 8 s, at room temperature (RT) and a pressure of 1 Torr. The second method used UV light from a mercury lamp within a UVO-cleaner kit (Model 42, Jelight Company Inc.) to generate ozone from ambient air directly above the diamond sample surface. Ozone reacted with the diamond surface at RT, oxidising it over a period of about 25 mins to achieve a full monolayer (ML) coverage. The third method involved refluxing the sample in a hot mixture of 100 ml H_2SO_4 (95%) with 6.5 g KNO_3 for 1 h at ~220 °C, followed by rinsing in deionised water and drying in N_2 gas. The fourth method, O_2 cracking, was performed in the deposition chamber of the NanoESCA facility *via* a thermal Mantis MGC75 gas cracker at a base pressure of ~2.2×10^{-6} mbar for 2 h. O_2 gas with a flow rate of 0.15 sccm was bled into the chamber and dissociated at a capillary power of 65 W to create O atoms, which then reacted with and oxidised the nearby RT diamond surface.

2.2. Surface analysis

SPA-LEED measurements were carried out using an electron energy of 100 eV or 130 eV for the H- and O-terminated SCD (100) samples, respectively. A simulation of the LEED pattern was generated using the *LEEDpat4* software [26] for each surface to aid the analysis of the experimental data.

High resolution X-ray spectroscopy was performed using a monochromatic Al Kα source (1486.7 eV) operating at 15 kV and 18 mA (270

W). A Scienta Omicron Argus analyser was situated at an electron polar angle of 45° to the surface normal. The total energy resolution was 600 meV at a pass energy of 20 eV for all high-resolution spectra.

Work function (WF) mapping and region-selected UPS spectra were obtained using EF-PEEM with an energy resolution of 0.14 eV. A Hg-vapour lamp ($h\nu < 5.8$ eV) and monochromatic He(I) discharge lamp (21.22 eV) were used as the UV-light source for WF mapping and UPS, respectively. Iris tuning allowed the field of view value of ~37.5 µm to be defined for the EF-PEEM study.

3. Results and discussion

3.1. Surface Structure

To assess the quality and structure of the oxidised diamond (100) surfaces, SPA-LEED was performed on *all* four samples. However, in order to have a benchmark for the oxidised diamond surfaces, the hydrogenated SCD (100) samples were first studied, and the results are given in detail in Section S1 in the Supplementary Information. The subsequent analysis of the oxidised samples revealed that the oxygen termination results in a reduction in symmetry and a change in the diffraction pattern compared to that for H-terminated diamond (Fig. S1 (a) in the Supplementary Information). As expected, *all* oxidised samples exhibit a distinctive (1 × 1) LEED pattern, consisting of a single 90°-rotated domain in a square lattice [27,28], as seen in Fig. 1 (a)–(d). However, the intensities of the first-order domains and background differs between oxidation techniques, resulting in variations in surface quality and roughness. The UV-ozone oxidation technique led to a highly ordered surface structure which manifested as sharp (1 × 1) domains and minimal background intensity, surpassing the LEED patterns observed using other oxidation techniques (Fig. 1(b)). In contrast, as shown in Fig. 1(c), the O_2-cracking method produced a LEED pattern with a weaker background intensity and less distinct spots compared to the other three methods. This difference can be attributed to the roughness and damage to the surface that occurred during the thermal cracking process [28]. The findings from the LEED studies were later corroborated by EF-PEEM maps, which will be presented in more detail in section 3.3.

The experimental SPA-LEED data for the oxygenated diamond (100) samples were verified by the *LEEDpat* software simulation, resulting in predictions of real and reciprocal-space patterns. The (1 × 1) structure for the O-terminated diamond was constructed using a single-domain matrix ($M = \begin{bmatrix} 1 & 0 \\ 0 & 1 \end{bmatrix}$) rotated by 90°. The reciprocal unit-cell vectors represent the two O adatoms, while the primitive unit-cell lattice is square, as expected for the O-terminated diamond (100) with a (1 × 1) reconstructed surface, as shown in Fig. 1(e) and (f), respectively.

3.2. Chemical composition

The effect of various oxidation methods on the oxygen-bonding configuration for the SCD (100) surface was evaluated using core-level XPS. The XPS analysis was performed using the *XPSPEAK41* software (version 4.1) and verified with the well-established fitting program, *CasaXPS* (version 2.3.18) [29], to achieve reproducible Gaussian-Lorentzian line profiles, GL(X), with a Shirley background [30]. The line profiles, labelled as GL(X), are fitted using a combination sum of Y% Gaussian + X% Lorentzian line shapes, where $X + Y = 100\%$. The combination of these two functions that provided the most accurate fit for the symmetric peak shape (*i.e.* C 1s and O 1s) depended upon the instrumental response (*i.e.* the X-ray line-shape of the core hole, pass energy, thermal broadening, *etc.*). The C 1s peak fitting required a smaller Lorentzian content of GL(28) compared to that of the H-terminated diamond (100) (see Fig. S2), while the O 1s lines were fitted best with a value of GL(35). It is crucial to consider that the presence of only C 1s and O 1s signals confirms the successful surface cleaning and lack of
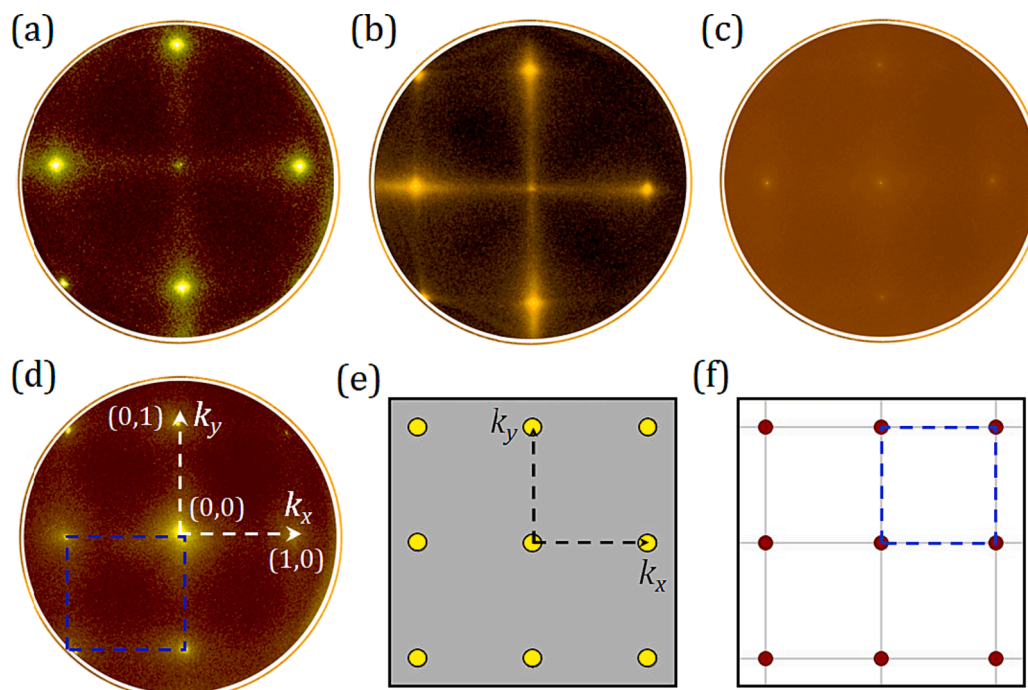
Fig. 1. Reciprocal-space LEED patterns obtained at a beam energy of 130 eV of the oxidised diamond (100) surfaces oxidised using (a) oxygen plasma, (b) UV-ozone, (c) acid oxidation and (d) oxygen cracking, respectively. In panel (d), white dashed arrows indicate the primitive reciprocal-lattice vectors along the k_x and k_y axes, while the blue dashed square corresponds to a (1×1) diffraction symmetry. Drawings of a superposition of the simulated reciprocal- and real-space patterns for C(1×1)-(100):O are illustrated in panels (e) and (f), respectively. In panel (e), yellow circles refer to the (1×1) domains in a square lattice, while black dashed arrows are the primitive reciprocal-lattice vectors showing (1×1) diffraction spots. In panel (f), the red circles indicate the position of individual domains, whilst the blue dashed square shows the (1×1) geometry.

contamination.

The deconvoluted C 1*s* peak is commonly utilised in the context of oxidised diamond to identify the nature of surface bonding [31,32]. The C 1*s* peak in a fully oxidised (100) diamond sample is decomposed into four distinct contributions, consistent with previous studies [16,18,31,33]. Fig. 2 highlights the prominent peaks observed in the C 1*s* peak lines for the oxygenated diamond (100) surface, which vary with different oxidation methods. The dominant peak in each spectrum remains unchanged, regardless of how the surface is terminated. This peak (labelled C1) has a binding energy (BE) of ~285.2 eV, and is assigned to bulk sp^3-hybridised C_d atoms. Due to the oxidised surface, a lower intensity peak (C2) at ~283.8 eV is present, attributed to graphitic or amorphous carbon, indicative of sp^2 C=C groups on the surface. For oxygenated diamond, typically three extra peaks can be detected at higher BEs. Notably, the intensity of these peaks can vary depending on the oxidation techniques used. The first peak (C3) at 286.6 eV is ascribed to the C_d–O single bonds present in ether (C_d–O–C_d) and hydroxyl (C_d–OH) functionalities. The second and third peaks (grouped together under the label C4) usually arise around ~288 eV and ~289 eV, and are associated with the C_d=O double bonds of carbonyl (*i.e.* ketone) and carboxyl (R-COOH) components, respectively, as reported by Ferro *et al.* [34]. In our samples, the carboxyl-group peak is relatively small because the C=O double bonds are primarily due to the ketone component.

Alternatively, if the surface is only partially oxidised, the presence of a fifth (C5) component can appear, indicating the existence of C_d–H bonds at the surface, as illustrated in the case of O_2 cracking (Fig. 2(c)). Spectral peak contributions of C 1*s*, with corresponding assignments, are listed in Table 1, for *all* oxidised diamond (100) samples.

Besides the core-level spectra of C 1*s*, the O 1*s* peak was also examined to evaluate its peak contributions to surface carbon-oxygen bonding. The O 1*s* spectra are typically observed within the BE range of 529 eV to 535 eV, and the positions of the peaks are dependent on the material bonding state. In general, the BE of the oxygen atom influences

the charge and bonding nature of O, therefore higher BE corresponds to a less negative charge and more pronounced single-bonded features of the oxygen-to-carbon bond.

Deconvolution of the O 1*s* peak in oxidised single-crystalline and nanocrystalline diamond has been widely reported resulting in two or three distinct components, each with a specific attribution. However, the findings from the two-component fitting analysis have been contradictory, as demonstrated by the conflicting assignments reported in prior works. For example, Lesiak *et al.* [35] attributed the two components to C_d–OH and C_d=O (ketone) bonds, while others proposed that they originated from C_d–OH and C_d–O–C_d bonds [36,37]. By performing three-component peak fitting, the fitting accuracy for oxygenated ultrananocrystalline and microcrystalline diamond samples was improved [18,38], assigning the 3 components to C_d=O, C_d–OH and C_d–O–C_d functional groups.

In this study, three-component peak fitting was similarly applied with C_d=O centred at 531.1 eV, C_d–OH around 532 eV, and C_d–O–C_d at ~532.7 eV, labelled as O1, O2 and O3 peaks, respectively, in Table 1 and Fig. 3.

To obtain a more nuanced evaluation of the surface chemical compositions of the oxygenated diamond (100) samples, the relative concentrations of C and O were then determined from the deconvoluted C 1*s* and O 1*s* peaks (see Table 2). This information provides valuable insight into the elemental composition of the oxygenated SCD samples and can aid in the interpretation of their properties and behaviour.

The atomic content of O in the oxidised layer was quantified by referencing the total peak area of C 1*s* and taking into account the relevant XPS sensitivity factors (*F*):

$$O\% = \frac{A(O_{1s})/F(O_{1s})}{[A(O_{1s})/F(O_{1s}) + A(C_{1s})/F(C_{1s})]} \times 100\% \qquad (1)$$

where A is total peak area, $F(O_{1s})$ and $F(C_{1s})$ are equal to 0.632 and 0.205, respectively, which were obtained using the known cross-
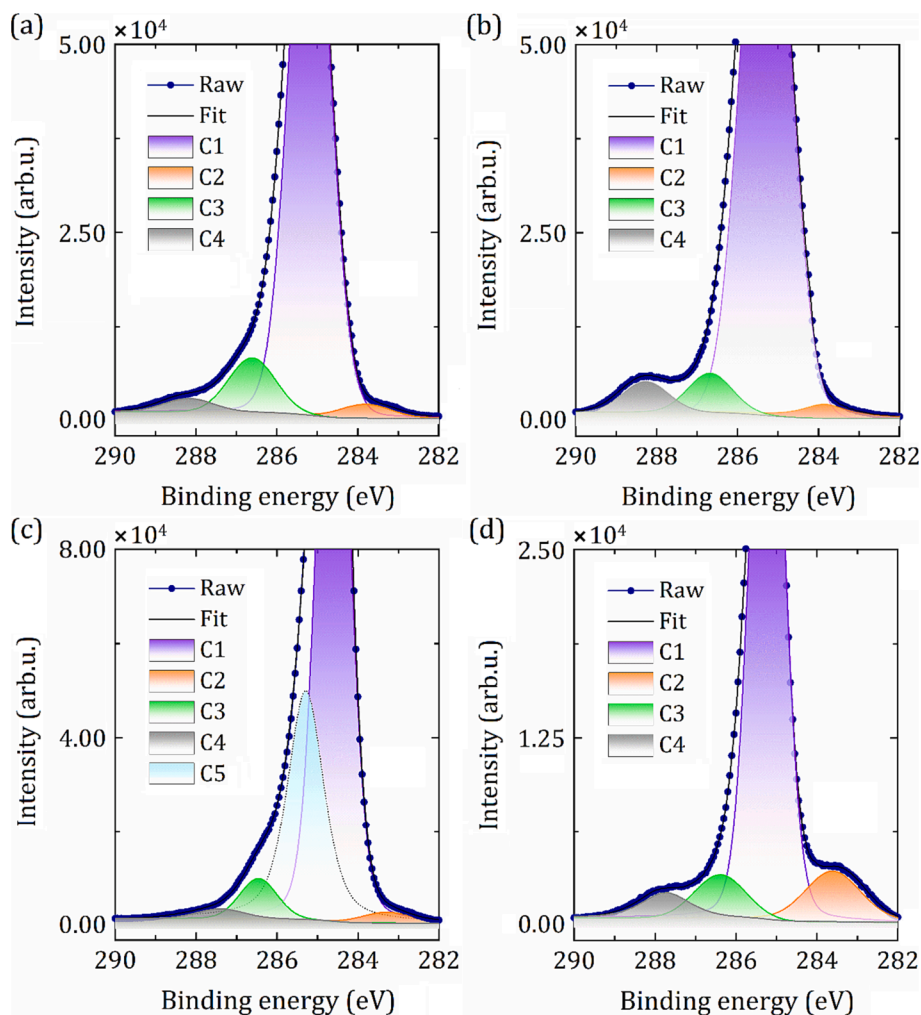
Fig. 2. Core-level XPS spectra from C 1*s* showing the raw experimental data and the fitted line-shape, as well as its deconvolution into contributions from peaks C1-C5 (see Table 1) as a function of oxidation method: (a) plasma oxidation, (b) UV-ozone, (c) oxygen cracking and (d) acid treatment. The tops of the C 1*s* peaks are cut off to highlight low-intensity components.

Table 1

Spectral fitting attributes (*e.g.* peak assignment and BE) of the C 1*s* and O 1*s* peaks for the four different oxidation techniques. *All* XPS spectra assignments are taken from Fig. 2 and Fig. 3 for C 1*s* and O 1*s*, respectively.

Spectra attributes		O_2 plasma	UV-ozone	O_2 cracking	Acid oxidation
		C 1*s*			
Peak	Assignment	BE / eV	BE / eV	BE / eV	BE / eV
C1	Bulk sp^3 C_d–C_d	285.2	285.3	284.6	285.2
C2	Surface sp^2 C=C	283.8	283.9	283.3	283.6
C3	C_d–O	286.6	286.7	286.5	286.4
C4	C_d=O	288.2	288.3	287.4	287.7
C5	Surface sp^3 C_d–C_d	–	–	285.3	–
		O 1*s*			
O1	C_d=O	531.1	531.1	531.1	531.1
O2	C_d–OH	532	531.9	532	531.9
O3	C_d–O–C_d	532.7	532.6	532.8	532.7

sectional area and asymmetry parameter values [39]. The calculation of O% in the oxidised layer using Eqn. (1) assumes a uniform distribution of O concentration in the layer, although the actual percentage may be lower due to the presence of C_d–C_d bonds in the diamond. To account for this, the calculation must take into account a few carbon layers, as the

inelastic mean free path (IMFP) of diamond upon exposure to Al Kα radiation is ~2.5 nm [40].

In Table 2, the maximum oxygen content of 10.4% was obtained after acid oxidation, whereas oxygen plasma and UV irradiation of the H-terminated samples produced 7.43% and 7.58% of O, assuming the surface was fully covered (see the Supplementary Information, Section S2). In contrast, the O_2-cracking treatment in a high-vacuum environment yielded the smallest recorded O coverage of 4.3% (or 0.57 ML), despite the thermal gas cracking conditions being the same as those reported by Wan *et al.* [28].

For ease of comparison, Fig. 4 presents a visual summary of the relative percentages of chemical compositions for the C 1*s* and O 1*s* core-level spectra in the O-terminated diamond taken from Table 2. Fig. 4(a) shows that the highest oxygen content obtained from acid oxidation is consistent with those reported from prior works [16,18,37,41], as the extent of diamond oxidation was influenced by various factors, such as the H_2SO_4/HNO_3 ratio, temperature, and duration. Different reaction pathways of diamond oxidation by a boiling acid mixture have been described elsewhere [18]. To the best of our knowledge, the oxygen concentration obtained with wet-chemical oxidation of single-crystal surfaces is among the highest values reported to date [16,18,37]. Additionally, the acid treatment resulted in a remarkable increase in the concentration of sp^2-bonded C (10.2%) compared to the other three methods. This suggests that the H-terminated SCD surface underwent significant etching during the oxidation process, leading to the
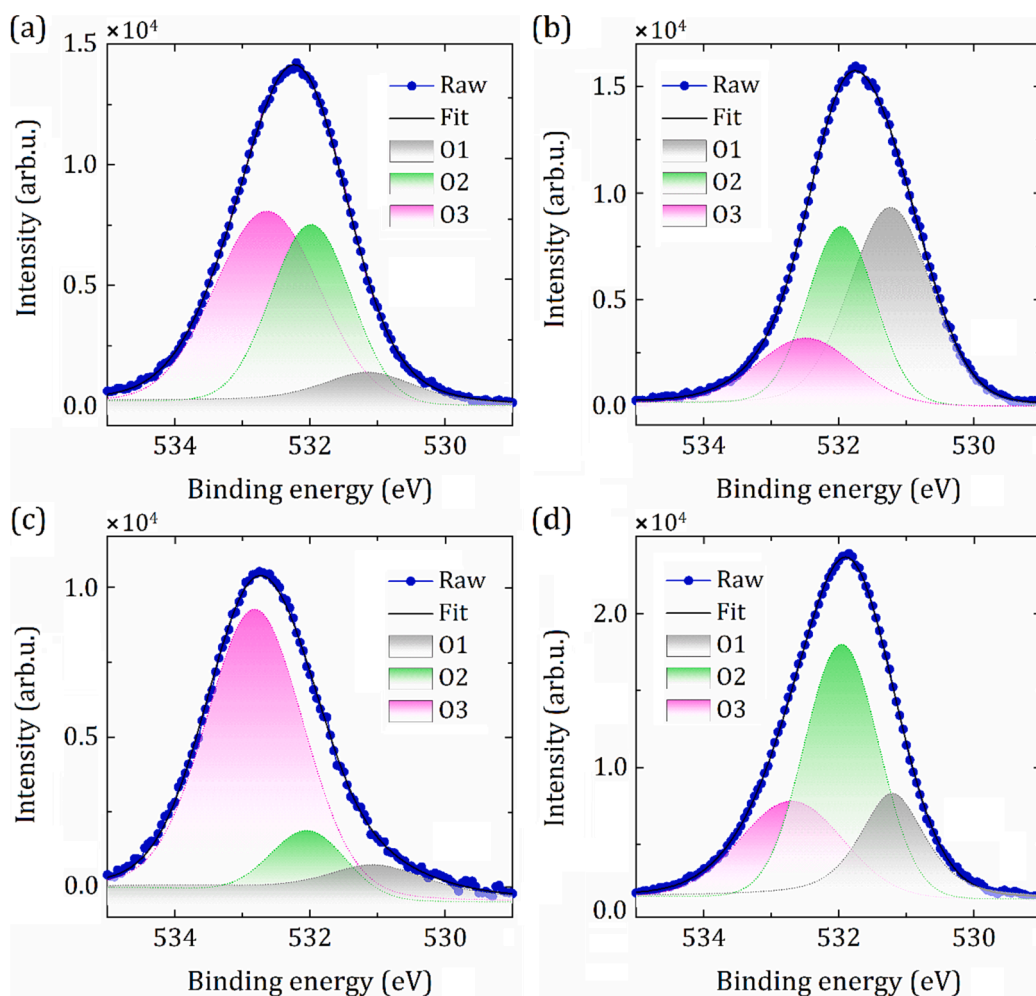
Fig. 3. Core-level XPS spectra of O 1*s* with corresponding peak components for O1-O3 (see Table 1) for different oxidation methods: (a) plasma oxidation, (b) UV-ozone, (c) oxygen cracking and (d) acid treatment.

Table 2
Relative surface compositions of C and O and their different surface structures for the oxygenated diamond (100) samples, as determined from C 1*s* and O 1*s* core-level XPS spectra. Note that the analysis is the outcome of a series of experiments, with each oxidation method consisting of five identical samples. The mean values were taken with the error limits of 0.1-0.7% for each chemical composition.

Method	Relative surface composition / %		Chemical compositions / %						
			C 1*s*				O 1*s*		
	C_d	O	$sp^{3 \text{ a}}$	sp^2	C_d–O	C_d=O	C_d–O–C_d	C_d–OH	C_d=O
O$_2$ plasma	92.6	7.4	87.9	3.6	6.8	1.7	52.1	37.1	10.8
UV-ozone	92.4	7.6	88.5	2.8	4.9	3.8	18.4	33.7	47.9
O$_2$ cracking	95.7	4.3	93.5 [a]	1.5	4.1	0.9	71.5	13.3	15.2
Acid oxidation	89.6	10.4	78.6	10.2	7.8	3.4	25.7	51.3	23.0

[a] Sum of bulk sp^3 and surface sp^3 carbons.

formation of a graphitic phase. These results are also consistent with previous findings [18,37], and they are further supported by the LEED pattern and the EF-PEEM map of acid oxidation (see sections 3.1 and 3.3).

To gain insights into the oxygen-containing functionalities, further analysis of the chemical components of the O 1*s* peak obtained through different oxidation techniques was conducted (Fig. 4(b)). The results show a range of oxidation levels and a diversity of functional groups (*i.e.* C_d–O–C_d, C_d–OH and C_d=O) present on the surface. In plasma oxidation, O$_2$ molecules are excited to higher energy states and ionised by energetic electrons in a DC field, and O$_2$ can also be dissociated into O atoms. The ionised species (O$_2^+$, O$^+$, *etc.*) are then accelerated onto the diamond

surface through the DC bias, colliding with neutral species (O atoms, O$_2$ molecules) along the way, and imparting downward motion to them *via* momentum transfer. Thus, the surface is bombarded with a range of ions and neutral species with high kinetic energy sufficient to overcome any activation barriers for oxidation reactions. O atoms, especially, having two dangling bonds, can react with the surface resulting in the formation of C_d–O–C_d groups, in agreement with prior studies [18,25].

In contrast, UV-ozone treatment involves the decomposition of ozone gas by UV light, producing both O$_2$ and atomic O. The kinetic energy of the atomic O generated through this process is significantly lower compared to those produced by the O plasma, thus atomic O reactions with the surface predominantly form C_d=O or C_d–OH functional groups
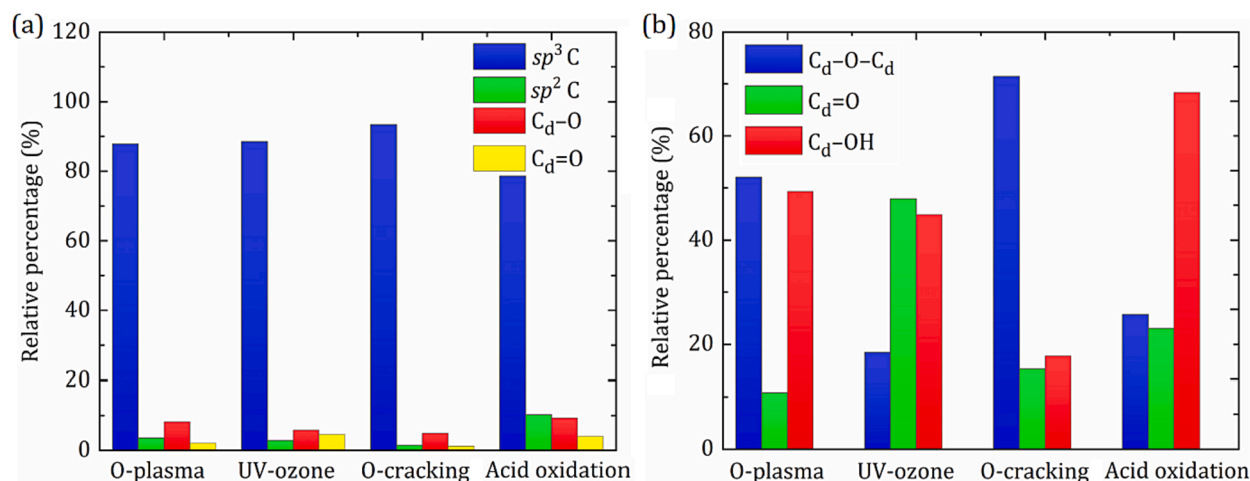
Fig. 4. Relative concentrations of the (a) C 1*s* and (b) O 1*s* components resulting from four distinct oxidation methods. The values are taken from Table 2.

[41,42].

In the case of O$_2$ cracking, the formation of atomic O is typically facilitated through thermal-energy-induced dissociation of O$_2$ molecules, which closely resembles the mechanism of plasma oxidation. This also results in the formation of C$_d$–O–C$_d$ bonds.

Finally, acid treatment of diamond typically leads to the production of a mixture of

C$_d$–OH and C$_d$=O groups, with a roughly equal ratio. This outcome is the result of a synergistic effect between the decomposition of the acid mixture and its reaction with the diamond surface.

Hydrogenated SCD (100) treated with the O$_2$-cracking method exhibits the highest concentration of C$_d$–O–C$_d$ bonds (71.5%) amongst other oxidation methods, as shown in Fig. 4(b). However, it is significant that the determination of ether bonding for the O$_2$ cracking treatment may not be entirely reliable as only partial surface coverage (0.57 ML) has been achieved. Therefore, the next highest concentration of the

C$_d$–O–C$_d$ group (52.1%) obtained by the plasma treatment can be deemed a trustworthy estimate. In contrast, the concentrations of C$_d$–OH bonding following O$_2$ cracking (13.3%) and plasma treatment (37.1%) are less than that produced by acid oxidation (51.3%), as expected and consistent with the literature [18].

Considering the importance of the findings for ether and hydroxyl groups, a thorough analysis of the latter component (C$_d$=O) is imperative, as it has been determined through density functional theory (DFT) calculations in our previous study that Sc preferentially adsorbs on the ketone-oxygenated diamond (100), resulting in the highest adsorption energy and the largest NEA [43] yet reported. Wet-chemical oxidation has been traditionally the preferred method for inducing the formation of a carbon-oxygen double-bond on the oxidised diamond surface. However, acid oxidation of the H-terminated diamond surface produced a C$_d$=O concentration of only 23.0%, a decrease of 1.5 times compared to previous results [18]. By comparison, UV-ozone irradiation was found to yield the highest concentration of C$_d$=O bonds observed, reaching 47.9%. This result is consistent with the calculated amount of C$_d$=O groups (44%) from the deconvoluted C 1*s* peak. The results acquired from the chemical-composition analysis of the four O-terminated diamond samples set the stage for subsequent electronic and structural studies.

3.3. Electronic Structure

With a focus on gaining insights into the electronic structure of diamond, we now turn to the examination of the four oxygenated samples using a combination of EF-PEEM and UPS measurements. The WF maps generated by EF-PEEM scans provide a qualitative assessment of the sample surfaces at the microscopic level. Supplementing these data with comprehensive UPS analysis yields valuable insights into the interplay between the valence band (VB) density-of-states (DOS) and chemical-bonding states in the region of interest. Utilising these two different methods, the WF values of the O-terminated SCD (100) samples were determined and compared.

The average WF values for the oxidised diamond (100) surfaces are presented in Fig. 5, depicted through colour-coded maps. Notably, the WF magnitudes of the O-terminated SCD (100) samples exhibit significant variation, ranging from 4.57 ± 0.02 eV to 5.92 ± 0.02 eV, depending on the oxidation technique used (see Table 3). To create a colour-coded map of the real-space WF data acquired across the sample surface, the EF-PEEM images in the area of interest were selected pixel by pixel, following the procedure outlined in Ref. [10]. The photoemission threshold for each pixel in the map was calculated using Eqn. (2):

$$I = \frac{I_{\max}}{2}\mathrm{erfc}\left(\frac{\phi - (E - E_{\mathrm{F}})}{\sigma\sqrt{2}}\right) + I_{\mathrm{off}} \qquad (2)$$

where $I_{\max}$ is the maximum intensity of each pixel, I_{off} is the intensity offset, ϕ is the average WF and σ is the standard deviation of the Gaussian distribution resulting from the energy broadening [44].

In contrast to the H-terminated (100) surface from Fig. S3(b), the colour-coded maps of *all* oxidised diamond samples, excluding the UV-ozone-treated one, show inhomogeneity with micron-sized blemishes appearing across the surface. This is not surprising, as O-termination typically results in etching (or even damaging) of the sample surface due to the reactive nature of atomic oxygen generated by various oxidation techniques [45,46]. Although the O-terminated sample produced by O$_2$ cracking displays a significantly lower WF (~4.73 eV) compared to samples oxidised by the other three methods, the single-crystal surface is probably damaged due to the high kinetic energy of the thermally cracked atomic fragments (Fig. 5(c)). Similarly, the O-terminated sample after acid oxidation exhibits a lower WF value of 5.04 eV and a substantially etched surface, as shown in Fig. 5(d). In contrast, the UV-ozone-treated sample exhibits the highest WF magnitude of ~5.92 eV among the samples studied, consistent with the previous study [24], despite the presence of only a few submicron spots on a highly uniform surface over a scale of 37.5 μm (Fig. 5(b)). Overall, the EF-PEEM results are in close agreement with the findings from the SPA-LEED study discussed in the previous section.

Fig. 6 presents the energy distribution of secondary electrons for the four oxidised (100) SCD samples, as determined by region-selected UPS analysis. This method also verifies the oxidation state of the samples. The oxidation of the H-terminated surface significantly reduces the intensity of the NEA peak at higher binding energies, as indicated by a comparison of the UPS spectra of the oxygenated surfaces in Fig. 6(a)
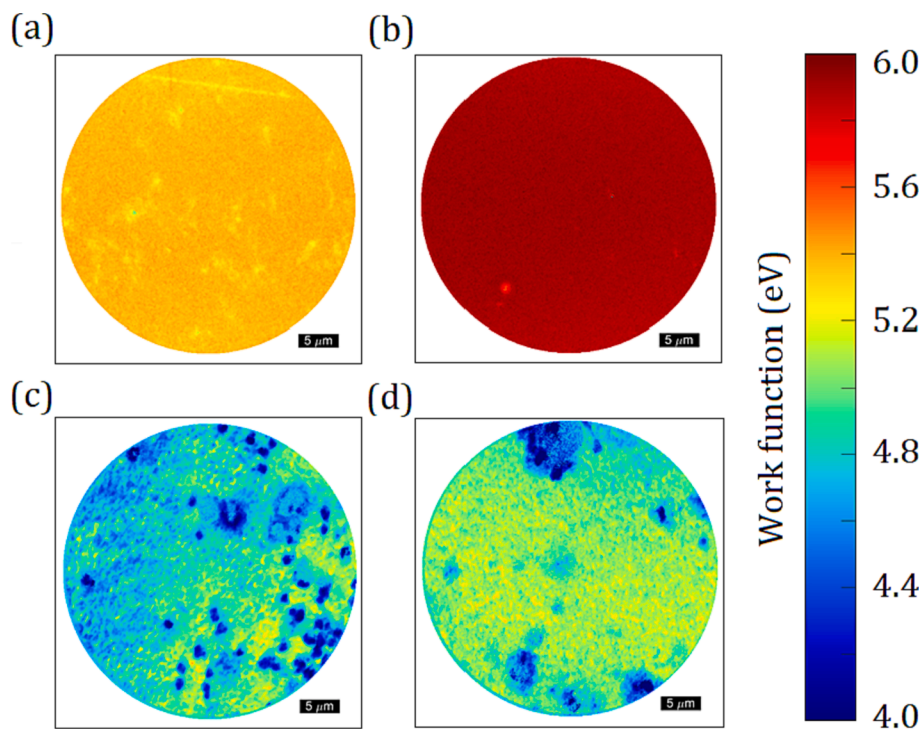
Fig. 5. Colour-coded work function maps of the four oxygenated single-crystal diamond (100) surfaces after treatment with (a) O_2 plasma, (b) UV-ozone, (c) O_2 cracking, and (d) acid oxidation. The field of view for each map is 37.5 μm.

Table 3
Experimentally determined values of the electronic structure of the O-terminated diamond (100) surfaces. Note: χ values are calculated from the results of the UPS analysis.

O-termination method	VBM / eV		ϕ / eV		χ / eV
	XPS	UPS[a]	UPS	EF-PEEM	
O_2 plasma	1.29	1.38	5.27	5.38	1.18
UV-ozone	1.37	1.42	5.79	5.92	1.74
O_2 cracking	0.68	1.03	4.65	4.73	0.21
Acid oxidation	1.33	1.36	4.93	5.04	0.82

[a] The values are indicated with a negative sign in Fig. 6(c), as the Fermi level is set to zero.

with those of the H-terminated diamond (100) sample from Fig. S3(a). In the UV-ozone-treated sample, for instance, the high cut-off energy is shifted to 15.41 eV, resulting in a kinetic-energy value that exceeds the band gap, characteristic of a surface with PEA [47]. Furthermore, intense valence band (VB) emissions observed at ~3.7 eV and 8.5 eV are attributed to O 2p states [48]. The intensity of these features changes depending upon the oxidation method used.

While EF-PEEM scans offer an averaged value of WF over a relatively larger surface area (up to 40 μm diameter), the UPS technique provides a more precise measurement of the WF in the region of interest. The full-scale UPS spectra for the O-terminated diamond (100) samples (Fig. 6 (a)) is divided into two regions of interest: region I corresponds to the conduction band (CB) states, and region II denotes the valence band (VB) states. A higher energy cut-off relative to the Fermi level (E_F) is determined by linear extrapolation in region I (Fig. 6(b)). In the same manner, the valence band maximum (VBM) position is calculated from the E_F position (Fig. 6(c)), as demonstrated previously [10,24,25]. Consequently, the WF of the O-terminated surfaces is calculated as the difference between the excitation energy of 21.22 eV (He(I)) and the cut-off energy, whilst the electron affinity, χ, is determined using Eqn. (3):

$$\chi = \phi + (E_F - E_{VBM}) - E_g \tag{3}$$

which considers the WF, ϕ, the position of the VBM relative to E_F, and the experimental band gap ($E_g = 5.47$ eV) for diamond. Experimentally measured values of ϕ (*i.e.* EF-PEEM and UPS) and the VBM (XPS and UPS) are tabulated in Table 3 alongside the electron affinity, χ, magnitudes. For *all* oxidised samples, the VBM from XPS analysis was calculated in the same manner as for the H-terminated surface (see Section S1) [9].

Although measured WF values from the UPS study were relatively lower than those obtained from EF-PEEM scans, the experimental results show a discrepancy of only around 2% between the two methods. Moreover, these findings demonstrate that the highest values of WF and EA, after UV-ozone oxidation, are 5.79 eV and 1.74 eV, respectively, in excellent agreement with prior work [47]. In contrast, the O_2-cracking method exhibits the lowest WF magnitude of 4.65 eV and a slight PEA of 0.21 eV. This is not surprising as the surface coverage was only partial, albeit exceeding half-monolayer coverage (0.57 ML), implying some H atoms at the surface were not fully replaced. In comparison, despite the O coverage for the acid treatment being greater than a full ML (1.38 ML), this sample has the next lowest WF value amongst the oxidation techniques.

The variation in the WF values between four different oxidation techniques can be attributed to the composition of specific components in the O termination. For example, acid oxidation had more than half (51.3%) of its chemical bonds as C_d–OH. As a result, according to the DFT study by Larsson [49], the OH-terminated BDD (100) surface possessed a lower WF value of 4.0 eV than that of the other two terminations, C_d–O–C_d (4.7 eV) and C_d=O (5.0 eV). This finding also accounts for why the O-terminated sample treated with the UV-ozone method exhibited the greatest WF value compared to those from other methods.

4. Conclusions

In this study, the surface oxidation of SCD (100) surfaces was studied using four distinct oxidation techniques, namely oxygen plasma, UV-ozone irradiation, acid treatment and oxygen thermal cracking. The oxidised samples underwent systematic analysis using various
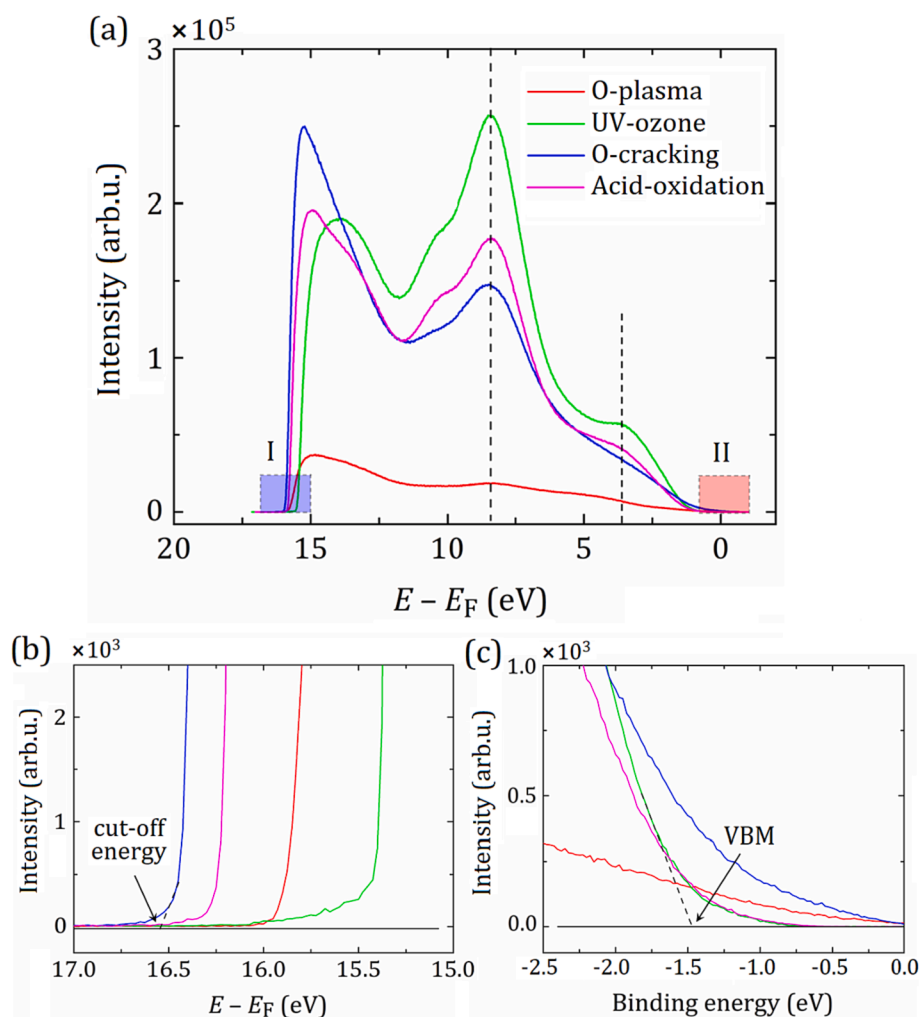
Fig. 6. Region-selected UPS spectra of the O-terminated diamond (100) surfaces: (a) the full-scale spectra labelled with two regions of interest, I and II, depicted with red and blue rectangles, respectively. These regions respectively correspond to the magnified panels of (b) the cut-off energy and (c) the VBM position relative to the Fermi level.

characterisation techniques (SPA-LEED, XPS, UPS, and EF-PEEM) to investigate the surface coverage, the concentrations of different carbon and oxygen components, as well as the surface electronic structure. The results obtained reveal that the electronic structure of O-terminated diamond (100) surfaces varies significantly depending on the oxidation technique used for surface treatment. Particularly, O_2-plasma and thermal-cracking methods yield more ether configurations (52.1% and 71.5%, respectively), while UV-ozone and acid-oxidation treatments favour ketone (47.9%) and hydroxyl (51.3%) groups. Moreover, the observed differences in the WF values of the four oxygenated diamond surfaces, which varied between 4.65 eV and 5.79 eV, were significantly influenced by oxygen-containing functional groups, consistent with earlier DFT predictions [49]. Thus, this finding reinforces the significant role of these functional groups in shaping the electronic properties of O-terminated diamond, which make it suitable not only for applications such as thermionic cathodes or vertical Schottky diodes (*i.e.* the metal-–O–C_d system) but also pave the way for the fabrication of quantum sensors utilising the nitrogen-vacancy (NV) centre in diamond.

Associated Content

Further details on this study can be found in the Supplementary Information file. The raw data for these experiments can be found in the University of Bristol data repository, data.bris, at https://doi.org/10.5523/bris.3b1g9byyd4v8h2udxh8be0s4ch.

CRediT authorship contribution statement

Ramiz Zulkharnay: Writing – review & editing, Writing – original draft, Methodology, Investigation, Formal analysis, Conceptualization. **Gulnur Zulpukarova:** Writing – review & editing, Validation, Investigation. **Paul W. May:** Writing – review & editing, Validation, Supervision, Methodology.

Declaration of competing interest

The authors declare that they have no known competing financial interests or personal relationships that could have appeared to influence the work reported in this paper.

Data availability

The raw data for these experiments can be found in the University of Bristol data repository, data.bris, at https://doi.org/10.5523/bris.3b1g9byyd4v8h2udxh8be0s4ch.

Acknowledgements

facility.

Appendix A. Supplementary data

Supplementary data to this article can be found online at https://doi.org/10.1016/j.apsusc.2024.159776.

References

[1] W. Yang, O. Auciello, J.E. Butler, W. Cai, J.A. Carlisle, J.E. Gerbi, D.M. Gruen, T. Knickerbocker, T.L. Lasseter, J.N. Russell, L.M. Smith, R.J. Hamers, DNA-modified nanocrystalline diamond thin-films as stable, biologically active substrates, Nat. Mater. 1 (4) (2002) 253–257.

[2] N. Yang, H. Uetsuka, E. Osawa, C.E. Nebel, Vertically aligned diamond nanowires for DNA sensing, Angew. Chem. Int. Ed. 47 (28) (2008) 5183–5185.

[3] A.D. Greentree, B.A. Fairchild, F.M. Hossain, S. Prawer, Diamond integrated quantum photonics, Mater. Today 11 (9) (2008) 22–31.

[4] N.P. de Leon, K.M. Itoh, D. Kim, K.K. Mehta, T.E. Northup, H. Paik, B.S. Palmer, N. Samarth, S. Sangtawesin, D.W. Steuerman, Materials challenges and opportunities for quantum computing hardware, Science 372 (6539) (2021) eabb2823.

[5] G. Zhang, R. Zulkharnay, X. Ke, M. Liao, L. Liu, Y. Guo, Y. Li, H.-G. Rubahn, V. V. Moshchalkov, P.W. May, Unconventional giant "Magnetoresistance" in bosonic semiconducting diamond nanorings, Adv. Mater. 35 (22) (2023) 2211129.

[6] M.F. Campbell, T.J. Celenza, F. Schmitt, J.W. Schwede, I. Bargatin, Progress toward high power output in thermionic energy converters, Adv. Sci. 8 (9) (2021) 2003812.

[7] M.C. James, F. Fogarty, R. Zulkharnay, N.A. Fox, P.W. May, A review of surface functionalisation of diamond for thermionic emission applications, Carbon 171 (2021) 532–550.

[8] V.S. Bormashov, S.Y. Troschiev, S.A. Tarelkin, A.P. Volkov, D.V. Teteruk, A. V. Golovanov, M.S. Kuznetsov, N.V. Kornilov, S.A. Terentiev, V.D. Blank, High power density nuclear battery prototype based on diamond Schottky diodes, Diam. Relat. Mater. 84 (2018) 41–47.

[9] F. Maier, J. Ristein, L. Ley, Electron affinity of plasma-hydrogenated and chemically oxidized diamond (100) surfaces, Phys. Rev. B 64 (2001) 165411.

[10] R. Zulkharnay, P.W. May, Experimental evidence for large negative electron affinity from scandium-terminated diamond, J. Mater. Chem. A 11 (25) (2023) 13432–13445.

[11] K. Okano, S. Koizumi, S.R.P. Silva, G.A.J. Amaratunga, Low-threshold cold cathodes made of nitrogen-doped chemical-vapour-deposited diamond, Nature 381 (6578) (1996) 140–141.

[12] A. Croot, G. Wan, A. Rowan, H.D. Andrade, J.A. Smith, N.A. Fox, Beta radiation enhanced thermionic emission from diamond thin films, Front Mech. Eng. 3 (2017) 1–8.

[13] G.R. Mackenzie, S. Kaluvan, P.G. Martin, C. Hutson, T. Connolley, M. Cattelan, H. Dominguez-Andrade, T.L. Martin, N.A. Fox, T.B. Scott, A diamond gammavoltaic cell utilizing surface conductivity and its response to different photon interaction mechanisms, Mater. Today Energy 21 (2021) 100688.

[14] H. Notsu, Introduction of oxygen-containing functional groups onto diamond electrode surfaces by oxygen plasma and anodic polarization, Electrochem. Solid-State Lett. 2 (10) (1999) 522.

[15] S. Torrengo, L. Minati, M. Filippi, A. Miotello, M. Ferrari, A. Chiasera, E. Vittone, A. Pasquarelli, M. Dipalo, E. Kohn, G. Speranza, XPS and UPS investigation of the diamond surface oxidation by UV irradiation, Diam. Relat. Mater 18 (5) (2009) 804–807.

[16] F. Klauser, S. Ghodbane, R. Boukherroub, S. Szunerits, D. Steinmüller-Nethl, E. Bertel, N. Memmel, Comparison of different oxidation techniques on single-crystal and nanocrystalline diamond surfaces, Diam. Relat. Mater. 19 (5) (2010) 474–478.

[17] X. Wang, A.R. Ruslinda, Y. Ishiyama, Y. Ishii, H. Kawarada, Higher coverage of carboxylic acid groups on oxidized single crystal diamond (001), Diam. Relat. Mater. 20 (10) (2011) 1319–1324.

[18] C. Li, X. Zhang, E.F. Oliveira, A.B. Puthirath, M.R. Neupane, J.D. Weil, A. G. Birdwell, T.G. Ivanov, S. Kong, T. Gray, H. Kannan, A. Biswas, R. Vajtai, D. S. Galvao, P.M. Ajayan, Systematic comparison of various oxidation treatments on diamond surface, Carbon 182 (2021) 725–734.

[19] I. Yagi, H. Notsu, T. Kondo, D.A. Tryk, A. Fujishima, Electrochemical selectivity for redox systems at oxygen-terminated diamond electrodes, J. Electroanal. Chem. 473 (1) (1999) 173–178.

[20] J.V. Macpherson, A practical guide to using boron doped diamond in electrochemical research, Phys. Chem. Chem. Phys. 17 (5) (2015) 2935–2949.

[21] T. Lechleitner, F. Klauser, T. Seppi, J. Lechner, P. Jennings, P. Perco, B. Mayer, D. Steinmüller-Nethl, J. Preiner, P. Hinterdorfer, M. Hermann, E. Bertel, K. Pfaller, W. Pfaller, The surface properties of nanocrystalline diamond and nanoparticulate diamond powder and their suitability as cell growth support surfaces, Biomaterials 29 (32) (2008) 4275–4284.

[22] P.W. May, E.M. Regan, A. Taylor, J. Uney, A.D. Dick, J. McGeehan, Spatially controlling neuronal adhesion on CVD diamond, Diam. Relat. Mater. 23 (2012) 100–104.

[23] P.A. Nistor, P.W. May, Diamond thin films: giving biomedical applications a new shine, J. R. Soc. Interface 14 (134) (2017) 20170382.

[24] M.C. James, M. Cattelan, N.A. Fox, R.F. Silva, R.M. Silva, P.W. May, Experimental studies of electron affinity and work function from aluminium on oxidized diamond (100) and (111) surfaces, Phys. Status Solidi B 258 (2021) 2100027.

[25] F. Fogarty, N.A. Fox, P.W. May, Experimental studies of electron affinity and work function from titanium on oxidised diamond (100) surfaces, Funct. Mater. 2 (1) (2022) 103–111.

[26] LEEDpat, V.4.2, K.E. Hermann, M.A.V. Hove, Berlin/Hong Kong see also http://www.fhi-berlin.mpg.de/KHsoftware/LEEDpat/index.html. (2014).

[27] P.E. Pehrsson, T.W. Mercer, Oxidation of the hydrogenated diamond (100) surface, Surf. Sci. 460 (1) (2000) 49–66.

[28] G. Wan, M. Cattelan, N.A. Fox, Electronic structure tunability of diamonds by surface functionalization, J. Phys. Chem. C 123 (7) (2019) 4168–4177.

[29] N. Fairley, V. Fernandez, M. Richard-Plouet, C. Guillot-Deudon, J. Walton, E. Smith, D. Flahaut, M. Greiner, M. Biesinger, S. Tougaard, D. Morgan, J. Baltrusaitis, Systematic and collaborative approach to problem solving using X-ray photoelectron spectroscopy, Appl. Surf. Sci. Adv. 5 (2021) 100112.

[30] D.A. Shirley, High-resolution X-ray photoemission spectrum of the valence bands of gold, Phys. Rev. B 5 (12) (1972) 4709–4714.

[31] S. Ghodbane, D. Ballutaud, A. Deneuville, C. Baron, Influence of boron concentration on the XPS spectra of the (100) surface of homoepitaxial boron-doped diamond films, Phys. Status Solidi A 203 (12) (2006) 3147–3151.

[32] G. Alba, M.P. Villar, R. Alcántara, J. Navas, D. Araujo, Surface states of (100) O-terminated diamond: towards other 1 × 1: O reconstruction models, Nanomaterials 10 (6) (2020) 1193.

[33] S. Torrengo, R. Canteri, R. Dell'Anna, L. Minati, A. Pasquarelli, G. Speranza, XPS and ToF-SIMS investigation of nanocrystalline diamond oxidized surfaces, Appl. Surf. Sci. 276 (2013) 101–111.

[34] S. Ferro, M. Dal Colle, A. De Battisti, Chemical surface characterization of electrochemically and thermally oxidized boron-doped diamond film electrodes, Carbon 43 (6) (2005) 1191–1203.

[35] B. Lesiak, L. Kövér, J. Tóth, J. Zemek, P. Jiricek, A. Kromka, N. Rangam, C sp2/sp3 hybridisations in carbon nanomaterials – XPS and (X)AES study, Appl. Surf. Sci. 452 (2018) 223–231.

[36] A. Gaisinskaya, R. Akhvlediani, R. Edrei, E. Alagem, Z. Joselzon, A. Hoffman, Chemical composition, thermal stability and hydrogen plasma treatment of laser-cut single-crystal diamond surface studied by X-ray photoelectron spectroscopy and atomic force microscopy, Diam. Relat. Mater. 19 (4) (2010) 305–313.

[37] J. Navas, D. Araujo, J.C. Piñero, A. Sánchez-Coronilla, E. Blanco, P. Villar, R. Alcántara, J. Montserrat, M. Florentin, D. Eon, J. Pernot, Oxygen termination of homoepitaxial diamond surface by ozone and chemical methods: An experimental and theoretical perspective, Appl. Surf. Sci. 433 (2018) 408–418.

[38] K. Huang, X. Hu, H. Xu, Y. Shen, A. Khomich, The oxidization behavior and mechanical properties of ultrananocrystalline diamond films at high temperature annealing, Appl. Surf. Sci. 317 (2014) 11–18.

[39] J.J. Yeh, I. Lindau, Atomic subshell photoionization cross sections and asymmetry parameters: $1 \leqslant Z \leqslant 103$, At. Data Nucl. Data Tables 32 (1) (1985) 1–155.

[40] H. Shinotsuka, S. Tanuma, C.J. Powell, D.R. Penn, Calculations of electron inelastic mean free paths. X. Data for 41 elemental solids over the 50 eV to 200 keV range with the relativistic full Penn algorithm, Surf. Interface Anal. 47 (9) (2015) 871–888.

[41] S. Ghodbane, T. Haensel, Y. Coffinier, S. Szunerits, D. Steinmüller-Nethl, R. Boukherroub, S.-I.-U. Ahmed, J.A. Schaefer, HREELS investigation of the surfaces of nanocrystalline diamond films oxidized by different processes, Langmuir 26 (24) (2010) 18798–18805.

[42] G. Speranza, S. Torrengo, M. Filippi, L. Minati, E. Vittone, A. Pasquarelli, M. Dipalo, E. Kohn, *In situ* thermal treatment of UV-oxidized diamond hydrogenated surface, Surf. Sci. 604 (9) (2010) 753–761.

[43] R. Zulkharnay, N.L. Allan, P.W. May, Ab initio study of negative electron affinity on the scandium-terminated diamond (100) surface for electron emission devices, Carbon 196 (2022) 176–185.

[44] H. Dominguez-Andrade, M.Z. Othman, K.M. O'Donnell, J.H. Lay, P.W. May, N. A. Fox, J. Morin, O. Renault, Use of energy-filtered photoelectron emission microscopy and Kelvin probe force microscopy to visualise work function changes on diamond thin films terminated with oxygen and lithium mono-layers for thermionic energy conversion, Int. J. Nanotechnol. 11 (9–1011) (2014) 796–807.

[45] F.K. de Theije, O. Roy, N.J. van der Laag, W.J.P. van Enckevort, Oxidative etching of diamond, Diam. Relat. Mater. 9 (3) (2000) 929–934.

[46] F. Silva, R.S. Sussmann, F. Bénédic, A. Gicquel, Reactive ion etching of diamond using microwave assisted plasmas, Diam. Relat. Mater. 12 (3) (2003) 369–373.

[47] G. Speranza, S. Torrengo, A. Miotello, L. Minati, I. Bernagozzi, M. Ferrari, M. Dipalo, E. Kohn, XPS and UPS *in situ* study of oxygen thermal desorption from nanocrystalline diamond surface oxidized by different process, Diam. Relat. Mater. 20 (4) (2011) 560–563.

[48] K.P. Loh, X.N. Xie, S.W. Yang, J.C. Zheng, Oxygen adsorption on (111)-oriented diamond: a study with ultraviolet photoelectron spectroscopy, temperature-programmed desorption, and periodic density functional theory, J. Phys. Chem. B 106 (20) (2002) 5230–5240.

[49] K. Larsson, The combined influence of dopant species and surface termination on the electronic properties of diamond surfaces, J. Carbon Res. 6 (2) (2020) 22.